Fast Scanning Nitrogen-Vacancy Magnetometry by Spectrum Demodulation

P. Welter,[1,2,†] B.A. Jósteinsson,[1,2,†] S. Josephy,[2] A. Wittmann,[3] A. Morales,[2]
G. Puebla-Hellmann,[2] and C.L. Degen[1,4,*]

[1]*Department of Physics, ETH Zürich, Otto Stern Weg 1, Zürich 8093, Switzerland*
[2]*QZabre AG, Regina-Kägi-Strasse 11, Zürich 8050, Switzerland*
[3]*Institute of Physics, Johannes Gutenberg Universität Mainz, Staudingerweg 7, Mainz 55128, Germany*
[4]*Quantum Center, ETH Zürich, Zürich 8093, Switzerland*

We demonstrate a spectrum demodulation technique allowing for rapid imaging in scanning nitrogen-vacancy center magnetometry. Our method relies on a periodic excitation of the electron spin resonance by wide-band frequency sweeps at a kilohertz rate combined with a phase-locked detection of the photoluminescence signal. The technique is robust against changes in spectrum shape and photoluminescence intensity, and is readily extended by a frequency feedback to enable real-time tracking of the spin resonance. Fast scanning magnetometry is especially useful for samples where the signal dynamic range is large, of order millitesla, such as for ferromagnets or ferrimagnets. We demonstrate our method by mapping stray fields above the model antiferromagnet α-Fe$_2$O$_3$ (hematite) at pixel rates of up to 100 Hz and an image resolution exceeding one megapixel.

I. INTRODUCTION

The scanning nitrogen-vacancy (N-V) magnetometer is a next-generation scanning probe microscope able to quantitatively map surface magnetic stray fields with sub-50-nm spatial resolution [1–4]. The technique relies on a single, optically readable defect spin embedded in a sharp diamond tip that is scanned over the sample of interest. Scanning N-V magnetometry exploits the principles of quantum metrology to reach very high sensitivities, leading to alternative opportunities in the imaging of weakly magnetic systems. In the recent past, scanning N-V magnetometry has been used to map the stray field of magnetic vortices and domain walls in ferromagnets [5–8], antiferromagnets [9–13] and multiferroics [14–16], skyrmions [17–20], superconducting vortices [21–23], and two-dimensional ferromagnetism [24–26].

In the most commonly used detection scheme, the spin resonance frequency f_0 of the N-V center is tracked using continuous-wave optically detected magnetic resonance (ODMR) spectroscopy, and later converted to units of magnetic field using the spin's gyromagnetic ratio ($\gamma_e = 2\pi \times 28$ GHz/T) [27]. In this scheme, the microwave excitation frequency is scanned slowly across the spin resonance and the resulting absorption line shape, detected using a photoluminescence (PL) measurement, fitted to

extract the resonance position. Although this scheme works well for slow acquisition speeds, the nonlinear least-squares fitting of the spectrum is computationally expensive and ill-suited for real-time performance past a few hertz. On the other hand, excitation of the resonance at a single or a few frequencies can be employed to simplify and speed up the data taking [2,28–30], at the cost of reduced stability against spectral changes and a narrow signal dynamic range. The possibility of acquiring a scan in a matter of minutes rather than hours or days is enticing, and would further bolster the versatility of the technique.

Several concepts for speeding up image acquisition have been presented in the past. These include qualitative approaches that rely on PL quenching [3] or fixed-frequency excitation [2], semiquantitative approaches using multifrequency excitation [31], resonance tracking [28], *a posteriori* field reconstruction [32], or combinations thereof [32]. The highest reported scan rates for single spin magnetometry are around 40 pixels/s in imaging [32] and 100 samples/s in stationary benchmarks [28]. For ensemble N-V sensing, real-time field tracking up to several hundred hertz has been reported [30,33,34].

In this work we present a signal demodulation method that easily scales to sample rates of 100 Hz and beyond, yet is directly quantitative without the need for postprocessing, and that can tolerate sudden jumps of the magnetic field. Our method is based on periodic excitation of the spin resonance by fast, wide-band frequency sweeps and spectral demodulation of the resulting PL signal. We also

*degenc@ethz.ch
†These authors contributed equally.

implement a real-time feedback to further increase the dynamic range. We demonstrate our technique by imaging the magnetic surface texture and domain structure of an antiferromagnetic thin film at pixel rates of up to 100 Hz.

II. TRADITIONAL RESONANCE DETECTION

The canonical detection method in ODMR involves slowly sweeping the microwave excitation frequency across the spin resonance and monitoring the optical PL emission [35]. By fitting of the resonance curve with an appropriate line shape, most often Lorentzian,

$$R(f) = R_0 \left[1 - \epsilon \left(1 + \frac{[f - f_0]^2}{\Gamma^2} \right)^{-1} \right], \quad (1)$$

the resonance frequency f_0 as well as other parameters including the resonance linewidth Γ, spin contrast ϵ, and PL emission rate R_0 can be extracted [Fig. 1(a)]. To avoid the computationally expensive fitting, the change in resonance frequency f_0 can also be detected by observing the change in amplitude ΔR at a single frequency f [blue dots in Fig. 1(a)]. This 'amplitude detection' can be extended to a few discrete frequency values to increase robustness [29]. Alternatively, a small (sublinewidth) modulation of the microwave frequency or bias field can be applied to record a differential line shape or to frequency lock to the resonance [28,36]. The above procedures work well for analyzing spectra at a slow rate or for detecting and tracking small $\delta f_0 < \Gamma$ changes in the resonance frequency. However, they are ill-suited for real-time tracking of large spectral shifts.

III. SPECTRUM DEMODULATION

In our spectrum demodulation method, the microwave drive $f(t)$ is swept quickly across a wide frequency window much larger than the resonance linewidth using a sawtooth frequency modulation. The modulation rate f_{mod} is chosen much faster than the intended integration time per spectrum, yet much slower than the absorption and repolarization rates of the spin. The recorded PL signal as a function of time $R(t)$ is then a periodic concatenation of (truncated) resonance line shapes [Fig. 1(b)]. By measuring the relative phase between the sawtooth drive $f(t)$ and the PL signal $R(t)$,

$$\phi = \frac{2\pi(f_0 - f_c)}{\Delta f_{\text{win}}}, \quad (2)$$

one can directly determine the frequency offset $f_0 - f_c$. Here, f_c is the center frequency and $\pm \Delta f_{\text{win}}/2$ the frequency span of the sawtooth modulation. Importantly, the phase ϕ is insensitive to the detailed line shape of the resonance.
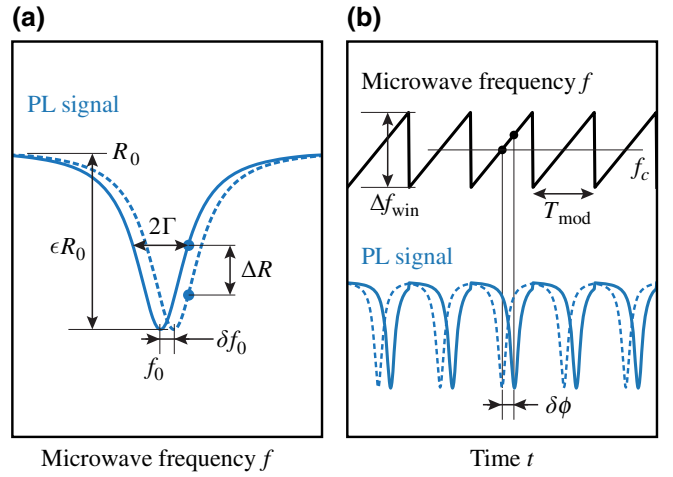

FIG. 1. (a) In traditional ODMR spectroscopy, the resonance frequency f_0 is estimated by fitting the spectral peak. Changes in magnetic field shift the position of the spectrum (dashed line). Here R_0 is the intensity of PL emission, ϵ the spin contrast, and Γ the linewidth parameter of the absorptive line shape. (b) In the spectrum demodulation technique, the spin resonance is excited periodically by fast microwave frequency sweeps (black sawtooth curve). The frequency modulation window Δf_{win} is chosen larger than Γ. A change in the spin resonance by δf_0 then causes a phase shift $\delta \phi = 2\pi \delta f_0 / \Delta f_{\text{win}}$ of the PL signal compared with the microwave drive (dashed line). The phase shift is measured by demodulating the PL signal, e.g., by a lock-in amplifier.

To experimentally determine ϕ, we demodulate $R(t)$ at the modulation frequency f_{mod} (for example, using a lock-in amplifier) and compute the argument of the in-phase and quadrature channels,

$$a_1 := \langle R(t) \cdot e^{2\pi i f_{\text{mod}} t} \rangle, \quad (3)$$

$$\phi = \arg(a_1) = \arctan(Y/X), \quad (4)$$

where the angled brackets represent an average or a low-pass filter to reject the image at $2f_{\text{mod}}$. Here $X = \text{Re}(a_1)$ and $Y = \text{Im}(a_1)$ are the in-phase and quadrature parts of the complex signal a_1, respectively. The desired frequency f_0 then follows from Eq. (2),

$$f_0 = f_c + \frac{\phi \Delta f_{\text{win}}}{2\pi}, \quad (5)$$

where the phase $\phi \in [-\pi, \pi[$.

The demodulation can be extended to higher harmonics nf_{mod} of $R(f)$, yielding a series of coefficients a_n. A shift of the resonance frequency results in phase shifts of $n\phi$ for the harmonic of order n. The expected amplitudes of higher harmonics are generally decreasing exponentially, therefore, phase measurements of the higher harmonics are increasingly noisy. Nevertheless, the higher harmonics can be included in the analysis to obtain an improved estimate

for f_0 (Appendices A and B). Furthermore, including harmonics up to second order allows extracting estimates for the resonance parameters Γ, ϵ, and R_0. For a Lorentzian line shape, these are given by (see Appendix A)

$$\Gamma \approx \frac{\Delta f_{\text{win}}}{2\pi} \ln \left| \frac{a_1}{a_2} \right|, \tag{6}$$

$$\epsilon \approx \frac{\Delta f_{\text{win}}}{\pi \Gamma} e^{2\pi \Gamma / \Delta f_{\text{win}}} \left| \frac{a_1}{a_0} \right|, \tag{7}$$

$$R_0 \approx a_0. \tag{8}$$

A more advanced analysis (Appendix B) also exploits phase information from the higher-order coefficients to improve the estimation of both the resonance frequency and the other parameters. However, in practice, Eqs. (6)–(8) already provide decent estimates for the resonance parameters.

IV. IMPLEMENTATION

A variety of ways may be devised to implement a spectrum demodulator. The key elements of the system are shown in Fig. 2 and include: (i) the demodulator itself, (ii) a data processing unit for extracting the resonance parameters, and (iii) optionally, a feedback to enable resonance tracking. In our system, the frequency modulation is generated on an arbitrary waveform generator, photodetection achieved via a single-photon avalanche photodiode (APD) and digital counter card, and all demodulation tasks are performed in software (see Sec. VII).

Many other implementations can be considered: a fully analog system may combine a linear avalanche photodiode (or a Geiger-mode APD with a downstream low-pass filter) with a lock-in amplifier and a proportional-integral-derivative (PID) controller. Conversely, a fully digital version may use a microprocessor to perform demodulation, signal extraction, and tracking in a single unit. Likewise, frequency modulation may be realized digitally (by direct digital synthesis) or fully analog (via a voltage-controlled oscillator).

V. SENSITIVITY

We next analyze the sensitivity of the spectrum demodulation technique and compare it to the conventional methods. The main source of noise in the optical detection system is photon shot noise. For low spin contrast $\epsilon \ll 1$, which is a good approximation for N-V centers, the noise is Poissonian and white and the power spectral density is simply given by $S = R_0$ [37]. Assuming a signal integration time of t_{int}, the equivalent noise bandwidth of the filter from Eq. (3) is $2/t_{\text{int}}$, and the variance of the demodulated signal is $\sigma^2 = R_0/t_{\text{int}}$. This variance is evenly distributed over both quadratures, $\sigma_X^2 = \sigma_Y^2 = R_0/2t_{\text{int}}$.
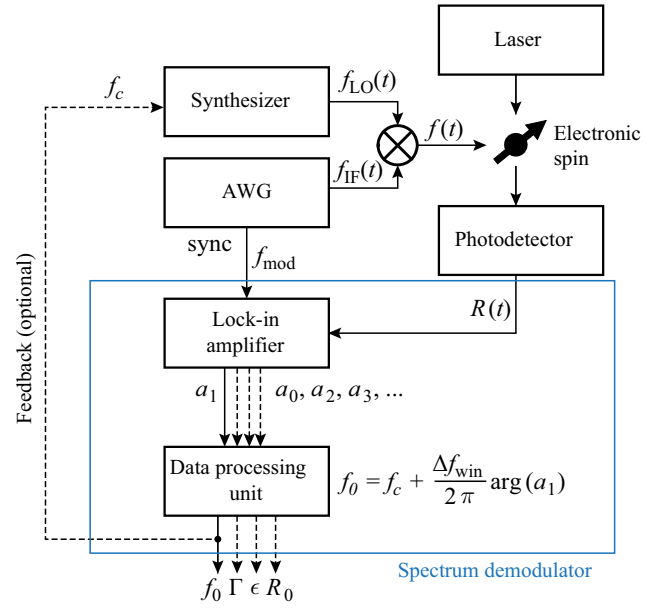

FIG. 2. Block diagram of the spectrum demodulator. The complete system consists of a conventional N-V magnetometer setup to which a demodulator is added (dashed blue box). The demodulator can be implemented in a variety of ways and always includes a lock-in amplifier and data processing unit. The lock-in amplifier computes the demodulated signals a_n, each representing the complex amplitude at the harmonic frequencies nf_{mod}. The data processing unit computes an estimate of the N-V resonance frequency f_0 (and possibly other parameters including R_0, ϵ, Γ) from the signals a_n. Data processing can be a simple arithmetic operation [Eqs. (4) and (5)], or can use advanced methods such as Kalman or particle filters for improved sensitivity. Resonance tracking may optionally be implemented by feeding back the estimate of the resonance frequency f_0 to dynamically adjust the center frequency f_c of the microwave modulation. In that case the spectrum demodulator together with the microwave synthesizer form a phase-locked loop that locks onto the N-V resonance frequency.

Next, we use Eqs. (4) and (5) to convert the uncertainties in X and Y into an uncertainty δf_0 of the estimated frequency shift (see Appendix A for derivation). The sensitivity η, defined as the uncertainty δf_0 normalized to unit time, is then given by

$$\eta = \delta f_0 \sqrt{t_{\text{int}}} \approx \frac{2\Gamma}{\epsilon \sqrt{R_0}} \times \frac{\alpha^2 e^{\pi/\alpha}}{\sqrt{2}\pi^2}. \tag{9}$$

Here, we introduce the relative window size $\alpha = \Delta f_{\text{win}}/(2\Gamma)$ as the ratio between Δf_{win} and 2Γ, and assume that $\alpha \gtrsim 1$.

It is instructive to compare Eq. (9) to the optimum sensitivity figure for amplitude detection [Fig. 1(a)] [38],

$$\eta \approx \frac{2\Gamma}{\epsilon \sqrt{R_0}} \times 0.77 \tag{10}$$

and to that of a least-squares fit (Appendix C),

$$\eta = \frac{2\Gamma}{\epsilon\sqrt{R_0}} \times \sqrt{2\alpha/\pi}. \tag{11}$$

Clearly, for small $\alpha \to 1$, the sensitivity of all techniques is similar. This is not surprising, because most frequency points lie in the vicinity of the resonance and contain useful information. Conversely, for $\alpha \gg 1$, the sensitivity rapidly ($\eta \propto \alpha^2$) deteriorates for our spectrum demodulation technique because the signal power is increasingly distributed over higher-harmonic coefficients a_n. In principle, the $\eta \propto \sqrt{\alpha}$ behavior of least-squares fitting can be recovered by including the a_n in the analysis, however, this comes at the cost of increased analytical complexity (Appendix B). Overall, the window size α is an important parameter in our spectrum demodulation technique, because it provides us with a knob to balance between a large signal range (large α) and a high sensitivity (small η).

VI. TRACKING

To combine a high sensitivity with a large signal range, it is useful to include a tracking method that dynamically recenters the frequency modulation window to the resonance position f_0, effectively forming a phase-locked loop. In our implementation, we adjust the center frequency f_c of the microwave drive to the last estimate for f_0 after every time step. Although more optimal and sophisticated tracking algorithms exist [39], we find this simple feedback to be satisfactory in most of our experiments.

Ultimately, the choice of window size Δf_{win} is a trade-off between signal-to-noise ratio (SNR) and tracking speed. The maximum frequency step allowed between two samples is given by $\Delta f_{\text{win}}/2$. This implies a maximum tracking rate (slew rate) for frequency jumps of

$$\text{SR} = \frac{\Delta f_{\text{win}}}{2t_{\text{int}}}. \tag{12}$$

Using parameters typical for the experiments presented below ($\Delta f_{\text{win}} = 30$ MHz, $t_{\text{int}} = 10$ ms, cf. Fig. 4), the maximum slew rate is approximately $\text{SR} = 1.5$ GHz/s corresponding to a magnetic slew rate of $2\pi/\gamma_e\text{SR} \sim 50$ mT/s.

VII. EXPERIMENTAL RESULTS

We experimentally demonstrate our spectrum demodulation technique using a commercial scanning magnetometer instrument (QSM, QZabre). The scanning magnetometer is equipped with an arbitrary waveform generator and local oscillator (LO) for microwave control, and a single-photon counting module for optical detection. We implement the frequency modulation by generating microwave chirp pulses at $f_{\text{mod}} = 1$ kHz around a 100 MHz baseband frequency, and mix it with the LO to the desired 2–4 GHz final frequency centered at f_c. We use an avalanche photodiode and a data acquisition card to count and bin the photons at a 20 μs dwell, corresponding to a data rate of 50 000 points per second. We demodulate the time trace in software by computing a fast Fourier transform of segments of duration t_{int} and retaining the coefficients corresponding to nf_{mod}. We then extract the resonance frequency f_0 from the phase of the first Fourier coefficient as per Eq. (5). Frequency tracking, when enabled, is implemented by updating the LO frequency according to the previously measured resonance frequency f_0. In our current implementation, there is substantial latency associated with this process (up to 10 ms), and in tracking mode we limit the maximum sample rate to 50 Hz. A future implementation will reduce this bottleneck by using an LO with lower latency.

We start experiments by assessing the sensitivity of the method. For this purpose, we record the resonance frequency f_0 at a constant rate given by t_{int} for a total of 200 samples without applying a magnetic signal. We then plot the standard deviation of the data record as a function of t_{int}. Figure 3(a) shows the measured standard deviation for four window sizes Δf_{win}. In all cases, the standard deviation scales with the inverse square root of t_{int}. This is expected from Eq. (A13) and confirms that the measurement is limited by shot noise. In Fig. 3(b) we plot the sensitivity η as a function of window size $\alpha = \Delta f_{\text{win}}/(2\Gamma)$. The experimental data matches the sensitivity model from Eq. (9) exceptionally well. Figure 3(b) also shows theory curves for least-squares fitting given by Eq. (11) as well as the lower bound imposed by Eq. (10). The best sensitivity achieved in Fig. 3(b) is approximately 4 μT/$\sqrt{\text{Hz}}$ for $\alpha \approx 2$, which is close to the theoretical limit of amplitude detection ($\eta = 2.2$ μT/$\sqrt{\text{Hz}}$).

To test the dynamic performance, we hover the scanning probe above a small copper coil ($\varnothing 5$ mm) and feed a current waveform through the coil. Figure 4 presents traces of the resulting coil magnetic field recorded at a rate of 50 Hz. For reference, we also show the applied waveform on a matching scale (orange trace). Figure 4(a) shows a trace recorded without tracking. Here, the dynamic range is limited to $\pm\frac{1}{2}\gamma_e\Delta f_{\text{win}} = \pm 0.53$ mT by the chosen window size of $\Delta f_{\text{win}} = 30$ MHz. Signals exceeding this range cannot be detected (not shown). Figure 4(b) shows a corresponding trace with the tracking enabled. The signal range is now much larger while the SNR is only marginally reduced (due to feedback latency). The fastest field change in Fig. 4(b) is approximately 28 mT/s, not far below the theoretical maximum of ca. 50 mT/s [Eq. (12)]. In both figures, gray bars indicate the instantaneous tracking window Δf_{win}.

Whether or not the tracking should be enabled depends on the expected signal magnitude. If the expected signal
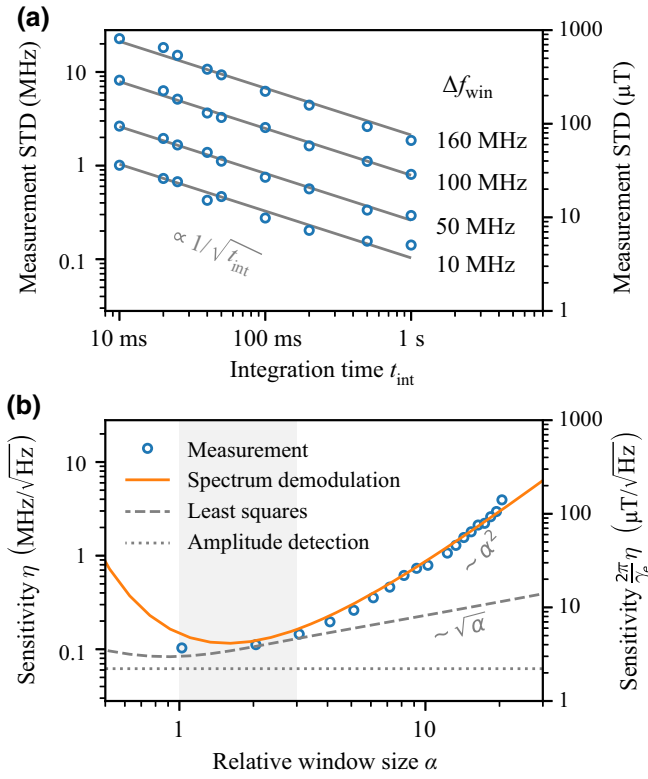
FIG. 3. (a) Experimental standard deviation of the demodulator frequency output f_0 computed from 200 data points with no magnetic field modulation applied, plotted as a function integration time t_{int} and window size Δf_{win}. The solid lines act as guides to the eye, illustrating that the uncertainty scales as $t_{int}^{-1/2}$ [Eq. (9)]. The right scale gives conversion to units of magnetic field. (b) Experimental sensitivity versus relative window size $\alpha = \Delta f_{win}/(2\Gamma)$. The solid gray curve is the theory scaling [Eq. (9)]. The dashed gray curve is the theory scaling for least-squares fitting [Eq. (11)]. The dotted gray curve is the theoretical limit for amplitude detection at the point of the steepest slope [Eq. (10)]. Gray shading indicates the range of optimum α. In this experiment, $R_0 \approx 500$ kCt/s, $\epsilon \approx 15\%$, and $2\Gamma \approx 10$ MHz.

dynamic range is small, less than approximately ± 30 MHz (equal to approximately ± 1 mT, i.e., 2 mT peak to peak), tracking is not necessary. The linewidth can be artificially broadened (or narrowed) by increasing (decreasing) the microwave power, such as to remain close to an optimum $\alpha \approx 3$. By contrast, if the expected signal is strong ($\gtrsim \pm 30$ MHz), tracking is recommended.

Finally, Fig. 5 shows images of the stray field above a magnetic thin film obtained by scanning magnetometry. The sample is a 10-nm film of α-Fe_2O_3 (hematite) grown epitaxially on an Al_2O_3 (001) substrate by off-axis magnetron sputtering capped with a 5 nm layer of Pt and a 2 nm layer of amorphous carbon. At room temperature, α-Fe_2O_3 exhibits weak ferromagnetism due to the canting of the antiferromagnetically coupled magnetic sublattices within the easy plane. The average domain size is of the order of
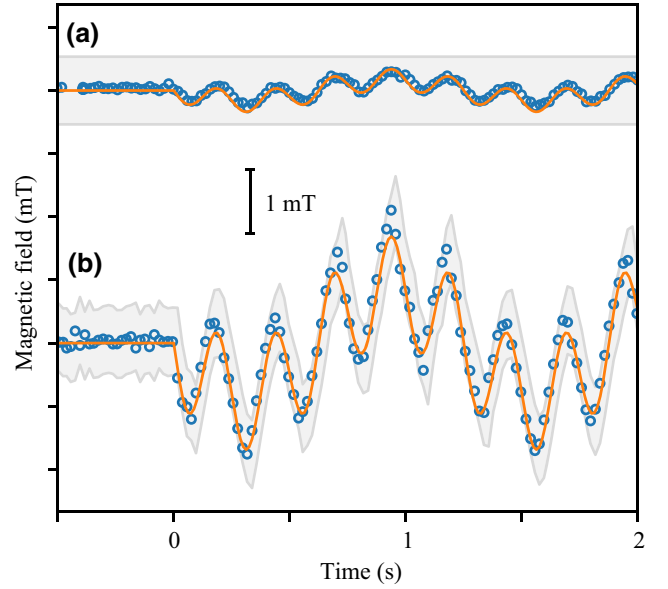

FIG. 4. Real-time monitoring of the magnetic field generated by passing a current through a coil underneath the N-V probe. (a) With resonance tracking disabled. (b) With resonance tracking enabled. The waveform starts at $t = 0$ s, and consists of two superimposed tones (0.8 and 4 Hz) with equal amplitude. Detection parameters are $R_0 \approx 950$ kCt/s, $\epsilon \approx 18\%$, $2\Gamma \approx 12$ MHz, and $\Delta f_{win} = 30$ MHz.

1 µm making it a suitable materials system for our demonstration [41]. The large image [Fig. 5(a)] is 1350×760 pixels, recorded at a rate of 100 Hz and resulting in a total measurement time of 3 h 5 min. Despite the fast acquisition rate and the fairly weak signal (approximately 500 µT peak to peak), the image shows exceptional detail and a high SNR. Figures 5(b)–5(f) show a 100×100 pixel subsection of the image recorded at different rates ranging from 2 to 100 Hz. Although some loss in SNR becomes visible at high rates, features are well resolved in all images while the total acquisition time is dramatically reduced from 1 h 28 min to below 2 min. For comparison, recording the large image at 2 Hz would have resulted in a scan time of approximately one week.

VIII. OUTLOOK

In summary, we discuss a technique for fast and quantitative spin resonance frequency estimation based on a combination of wide-band frequency modulation and lock-in detection. Among the advantages of our method are its inherent robustness against changes in the spectrum shape and PL intensity, while offering similar speed and sensitivity. A further useful feature is the ability to work in open-loop mode (without frequency tracking) and the possibility of tuning the frequency window (via the parameter α), allowing the user to choose between speed and dynamic range. In addition, resonance parameters including the PL
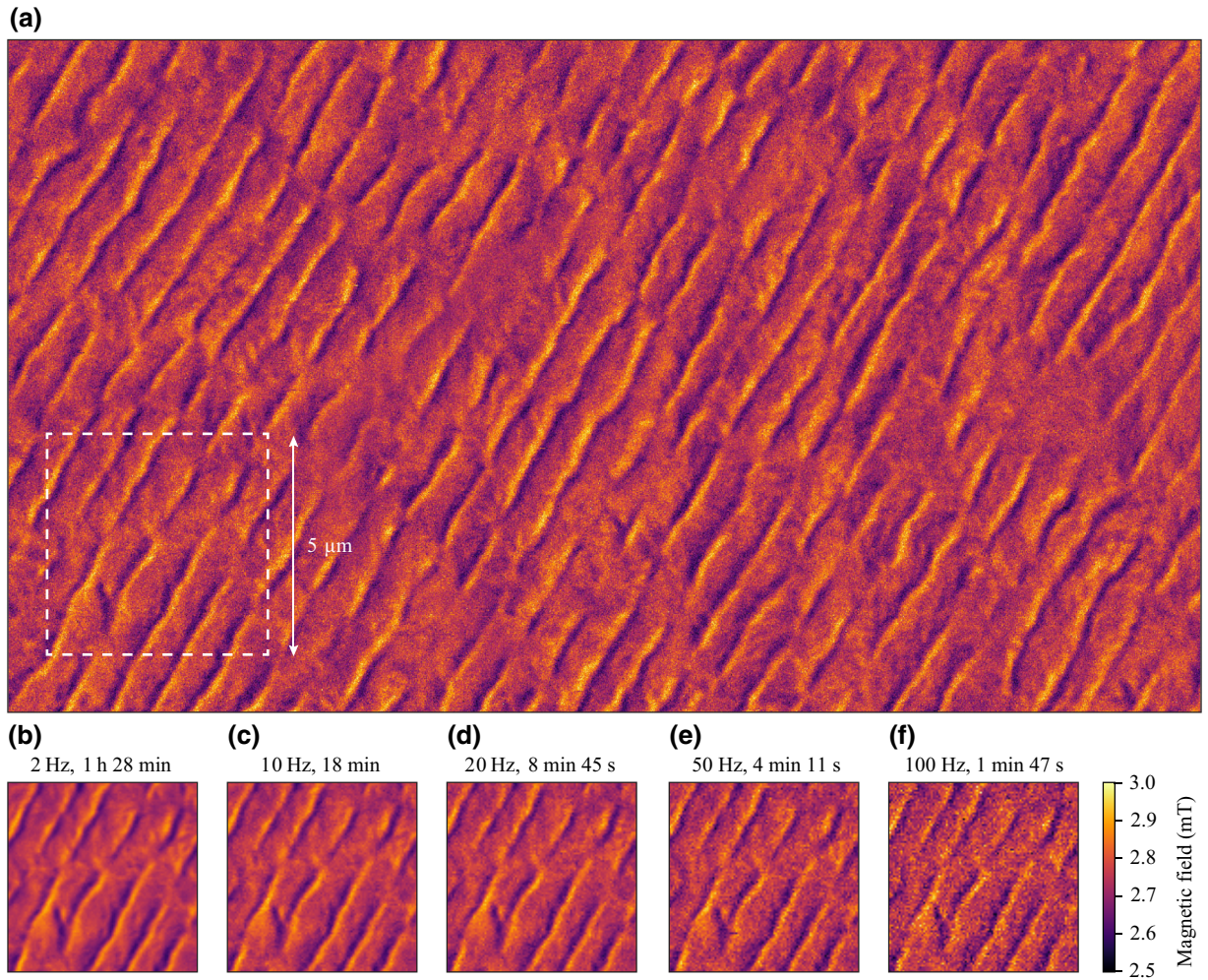
(a)

(b) 2 Hz, 1 h 28 min   **(c)** 10 Hz, 18 min   **(d)** 20 Hz, 8 min 45 s   **(e)** 50 Hz, 4 min 11 s   **(f)** 100 Hz, 1 min 47 s

FIG. 5. Magnetometry scans on α-Fe$_2$O$_3$ films using the spectrum demodulation technique. (a) Large-area scan (27×15.2 μm) containing 1.03 million pixels. Pixel rate is 100 Hz and spacing is 20 nm. Total scan time is 3 h 5 min. The diagonal stripe pattern is likely due to steps in the surface topography [40] while the large-scale structure reflects the magnetic domains. (b)–(f) 100×100 pixel scans recorded at varying rates, 2 to 100 Hz, in the region corresponding to the dashed rectangle in panel (a). Titles indicate the scan rate and the total acquisition time. Pixel spacing is 50 nm. Experimental parameters are $R_0 \approx 400$ KCt/s, $\epsilon \approx 20\%$, $2\Gamma \approx 11$ MHz, and $\Delta f_{\mathrm{win}} = 30$ MHz. A small bias field of ca. 2.75 mT is applied along the N-V symmetry axis.

intensity R_0, spin contrast ϵ, and linewidth Γ can be extract at no extra measurement cost. We demonstrate our technique by imaging the weak surface stray fields above the canted antiferromagnet α-Fe$_2$O$_3$, representing a wide class of weakly magnetic materials including antiferromagnets, ferrimagnets, and thin-film ferromagnets including two-dimensional ferromagnets. We demonstrate data rates of up to 100 Hz and image sizes of up to one megapixel.

Looking forward, the spectrum demodulation technique can be further improved in several directions. A simple extrapolation (Appendix D) indicates that the upper limit to the pixel rate is above 1 kHz for our experimental parameters, based on the available SNR. We currently do not reach this rate due to hardware latency. More advanced data processing and feedback techniques, such as the Kalman or particle filters [39], will also increase

sensitivity and robustness and will possibly allow for even faster rates. Furthermore, data can be postprocessed [32] to optimize the SNR after a scan has completed.

Another interesting future avenue is the implementation of gradiometry imaging. Recent work has demonstrated spectacular improvements to sensitivity and image quality in scanning experiments by detecting the magnetic field gradient [40]. Gradiometry relies on a mechanical oscillation of the sensor above the sample surface, which up-converts the local gradient into a time-varying field set by the oscillation frequency. While the original implementation relied on pulsed ac quantum sensing techniques, the concept can also be exploited in the context of the spectrum demodulation. Assuming the mechanical oscillation frequency is f_{TF}, magnetic field gradients will lead to signal sidebands at $f_{\mathrm{TF}} \pm nf_{\mathrm{mod}}$ in addition to the original

signal at nf_{mod}. For typical tuning fork oscillators, $f_{TF} \sim$ 32 kHz is much larger than $f_{mod} = 1$ kHz, therefore, signals are spectrally well separated. The gradient signal (and if desired, higher-order derivatives around multiples of f_{TF}) can be demodulated in exactly the same way as the standard demodulation technique (see Appendix E for details). Measuring the gradient in addition to the direct field takes no extra measurement time, the only resource consumed is additional computation time. In the particular case where the scanning probe oscillates in the direction of the fast scanning axis, an estimate of the gradient (even if noisy) neatly integrates with a recursive estimator, improving the dynamic prediction of the field at the next pixel.

APPENDIX A: DERIVATION OF SENSITIVITY

We aim to compute the sensitivity to frequency shifts based on a single coefficient a_1. We start by deriving an approximate analytical expression for a_1. Assume zero frequency shift ($f_c = f_0$). We define the sweep rate $v = f_{mod}\Delta f_{win}$ and the sweep period $T = 1/f_{mod}$. Over a single modulation period $|t| < T/2$, the luminescence time trace is simply the Lorentzian line shape

$$L(t) := R(vt + f_c) = R_0(1 - \epsilon[1 + (vt)^2/\Gamma^2]^{-1}), \quad (A1)$$

as per Eq. (1). We can use this expression to describe the luminescence time trace over multiple periods,

$$R(t) = \left(\sum_{n=-\infty}^{\infty} \delta(t - nT) \right) * \left(L(t)\, \mathrm{rect}(t/T) \right), \quad (A2)$$

where $\mathrm{rect}(t/T)$ is the rectangular function that truncates the Lorentzian. The convolution ($*$) with a delta comb then creates the periodic PL signal.

We next compute the Fourier transform of Eq. (A2),

$$\mathcal{F}[R(t)](f) = \left(\frac{1}{T} \sum_{k=-\infty}^{\infty} \delta\left(f - \frac{k}{T}\right) \right) \cdot \left(\mathcal{F}[L](f) * (T\,\mathrm{sinc}(Tf)) \right). \quad (A3)$$

Here, we apply that multiplication and convolution are dual operations under a Fourier transform, that the Fourier transform of a comb is another comb, and that the Fourier transform of $\mathrm{rect}(t)$ is a sinc function, $\mathrm{sinc}(x) = \sin(\pi x)/(\pi x)$. The Fourier transform of the Lorentzian is a double-sided exponential,

$$\mathcal{F}[L](f) = R_0\delta(f) - \frac{\pi R_0 \epsilon \Gamma}{v} e^{-2\pi\Gamma|f|/v}. \quad (A4)$$

Note that we use the following convention for defining the Fourier transform:

$$\mathcal{F}[g](f) := \int_{-\infty}^{\infty} g(t)e^{-2\pi ift}dt. \quad (A5)$$

In Eq. (A3), for frequencies no larger than a small multiple of f_{mod}, the sinc function is much sharper than the decaying exponential in Eq. (A4), and we approximate

$$T\mathrm{sinc}(Tf) \approx \delta(f). \quad (A6)$$

This approximation is equivalent to neglecting the truncation, noting that (i) the Lorentzian has largely decayed towards the side of the window, and (ii) the truncation creates a discontinuity that mostly contains higher frequencies ($\gg f_{mod}$) that are rejected by the demodulation. Combining Eqs. (A3), (A4), and (A6), we find that

$$\mathcal{F}[R(t)](f) = \left(\sum_{k=-\infty}^{\infty} \delta\left(f - \frac{k}{T}\right) \right) \cdot \left(\frac{R_0}{T}\delta(f) - \frac{\pi R_0 \epsilon \Gamma}{\Delta f_{win}} e^{-2\pi\Gamma|f|/v} \right). \quad (A7)$$

Here, the multiplication with the comb discretizes the spectrum of $R(t)$, as expected from its periodicity. Indeed, we can represent $\mathcal{F}[R(t)](f)$ as a Fourier series,

$$\mathcal{F}[R(t)](f) \stackrel{!}{=} \sum_{k=-\infty}^{\infty} a_k \delta(f - k/T). \quad (A8)$$

By comparison of coefficients, we find that

$$a_0 = R_0 - \frac{\pi R_0 \epsilon \Gamma}{\Delta f_{win}} \approx R_0, \quad (A9)$$

$$a_1 \approx \frac{\pi R_0 \epsilon \Gamma}{\Delta f_{\text{win}}} e^{-2\pi \Gamma f_{\text{mod}}/v} = \frac{\pi R_0 \epsilon \Gamma}{\Delta f_{\text{win}}} e^{-2\pi \Gamma/\Delta f_{\text{win}}}, \quad \text{(A10)}$$

$$a_2 \approx \frac{\pi R_0 \epsilon \Gamma}{\Delta f_{\text{win}}} e^{-4\pi \Gamma/\Delta f_{\text{win}}}. \quad \text{(A11)}$$

As expected, a_1 is purely real in the absence of a shift of f_0. Otherwise, by Eq. (2), a_1 is rotated in the complex plane by an angle ϕ. Since we know the magnitude $|a_1|$ from Eq. (A10), as well as its variance from shot noise ($\sigma_X^2 = \sigma_Y^2 = R_0/2t_{\text{int}}$, see main text), it is straightforward to compute the uncertainty in its phase, using standard error propagation,

$$\delta\phi = \frac{\sqrt{R_0/2t_{\text{int}}}}{|a_1|}. \quad \text{(A12)}$$

Equivalently, the uncertainty in estimated resonance frequency [cf. Eq. (5)] is given by

$$\delta f_0 = \delta\phi \frac{\Delta f_{\text{win}}}{2\pi} = \frac{2\Gamma}{\epsilon\sqrt{R_0}} \frac{\alpha^2 e^{\pi/\alpha}}{\sqrt{2}\pi^2} (t_{\text{int}})^{-1/2}. \quad \text{(A13)}$$

In the last step we have introduced the relative window size $\alpha = \Delta f_{\text{win}}/(2\Gamma)$. The sensitivity η, defined as the uncertainty in f_0 normalized to unit time, is given by

$$\eta = \delta f_0 \cdot \sqrt{t_{\text{int}}}, \quad \text{(A14)}$$

immediately yielding Eq. (9).

Solving Eqs. (A9)–(A11) for ϵ, Γ, and R_0 yields Eqs. (6)–(8),

$$a_0 \approx R_0, \quad \text{(A15)}$$

$$|a_1/a_2| = \exp(2\pi\Gamma/\Delta f_{\text{win}})$$

$$\Rightarrow \Gamma = \frac{\Delta f_{\text{win}}}{2\pi} \ln|a_1/a_2|, \quad \text{(A16)}$$

$$|a_1/a_0| \approx \frac{\pi\epsilon\Gamma}{\Delta f_{\text{win}}} e^{-2\pi\Gamma/\Delta f_{\text{win}}} = \frac{\pi\epsilon}{2\alpha} e^{-\pi/\alpha}$$

$$\Rightarrow \epsilon = \frac{2\alpha}{\pi} e^{\pi/\alpha} \left|\frac{a_1}{a_0}\right|. \quad \text{(A17)}$$

APPENDIX B: HIGHER-ORDER COEFFICIENTS

The phase of a_1 is a straightforward way to estimate the resonance frequency. But we can extend our analysis to include higher harmonics ($n f_{\text{mod}}$), allowing us to potentially improve sensitivity and extract information on Γ, ϵ, and R_0 at the same time. In the following, we will move from a continuous-time picture to discrete time, and assume we have sampled $R(t)$ on a regular grid t_k, with a sampling time $\Delta t = t_{\text{int}}/N$ and number of samples N. The harmonic coefficients up to $n = 2$ are given by

$$a_0 = \frac{1}{N} \sum_k R(t_k), \quad \text{(B1)}$$

$$a_1 = \frac{1}{N} \sum_k R(t_k) e^{2\pi i f_{\text{mod}} t_k}, \quad \text{(B2)}$$

$$a_2 = \frac{1}{N} \sum_k R(t_k) e^{2\pi i 2 f_{\text{mod}} t_k},$$

$$\cdots. \quad \text{(B3)}$$

Note how we also include the dc value a_0. Equation (B2) is the discrete-time analogue of Eq. (3).

A shift of the resonance frequency that results in a phase shift of a_1 by ϕ will shift a_2 by 2ϕ, and so on. The expected amplitudes of higher harmonics are generally decreasing exponentially (Appendix A), so measurements of the phase of the higher harmonics are increasingly noisy. Indeed, all coefficients have the same variance $\sigma^2 = R_0/t_{\text{int}}$, and, by the central limit theorem, their distribution is closely normal.

All of the coefficients a_j carry usable information about all of the parameters. For instance, Eqs. (6)–(8) clearly discard the phase information in a_2. The challenge is to find a suitable way to combine all of these measurements (real and imaginary part of each a_j) into a single estimate of all the parameters. Because all a_j satisfy the condition of being normally distributed with equal variances, the maximum-likelihood estimate is in fact the one produced by least-squares optimization. That is, the optimum estimate is

$$\hat{f}_0, \hat{\epsilon}, \hat{\Gamma}, \hat{R}_0 = \arg\min \sum_j |\tilde{a}_j - a_j|^2, \quad \text{(B4)}$$

where $\tilde{a}_j = \tilde{a}_j(f_0, \epsilon, \Gamma, R_0)$ represent the expected coefficients based on a model of the line shape, cf. Eqs. (A9)–(A11).

With the only difference that the raw data are first Fourier transformed, Eq. (B4) is equivalent to directly fitting the Lorentzian spectrum, a method we earlier dismissed as too computationally expensive. The key advantage here is that we can truncate the sum in Eq. (B4) at perhaps $n = 3$, as the remaining a_j are small and the information they carry is minimal. But indeed there is a trade-off to be made here, between computational complexity and sensitivity.

APPENDIX C: DERIVATION OF SENSITIVITY OF LEAST-SQUARES FITTING

Next, we aim to compare the uncertainty above in Eq. (A13) to the standard method of least-squares fitting the Lorentzian spectrum directly. A complete calculation of

the error propagation through a full nonlinear least-squares fitting operation is intractable and unlikely to yield any tangible insights. Instead, to simplify the calculations, we relax the requirements by making the following assumptions.

(a) We only fit the resonance frequency f_0, and assume that the linewidth Γ, contrast ϵ, and count rate R_0 are known exactly.

(b) We further assume that we already have a decent estimate of f_0, and we perform a single *linear* least-squares step starting from the true value f_0.

(c) Likewise, the window shall be well centered on the resonance, i.e., $f_c \approx f_0$.

Hence, the model function that we fit to our data is

$$R_{f_0}(f) = R_0(1 - \epsilon[1 + (f - f_0)^2/\Gamma^2]^{-1}). \quad (C1)$$

Our measurement is a noisy sample of this function,

$$y_k = R_{f_0}(f_k)\frac{t_{\text{int}}}{N} + w_k, \quad k = 1, \ldots, N. \quad (C2)$$

Here, we sample the spectrum at the frequencies f_k. The total integration time t_{int} is spread across all N points. The random variable $w_k \sim \mathcal{N}(0, \sigma^2 = R_o t_{\text{int}}/N)$ captures the shot noise.

The Jacobian of the least-squares problem reads

$$J_k = \frac{\partial R_{f_0}(f_k)}{\partial f_0} \frac{t_{\text{int}}}{N}. \quad (C3)$$

Note that because we are only fitting a single parameter f_0, the Jacobian is simply a row vector. Let $\hat{f}_0$ be the least-squares estimate of the resonance frequency. Its variance is given by

$$\mathbb{V}\left[\hat{f}_0\right] = \sigma^2 \left(J^{\mathsf{T}}J\right)^{-1} \quad (C4)$$

$$= \sigma^2 \left(\sum_{k=1}^{N} J_k^2\right)^{-1} \quad (C5)$$

$$= \sigma^2 \left(\sum_{k=1}^{N} \left(\frac{\partial R_{f_0}(f_k)}{\partial f_0} \frac{t_{\text{int}}}{N}\right)^2\right)^{-1} \quad (C6)$$

$$\approx \sigma^2 \left(\int_{f_c-\alpha\Gamma}^{f_c+\alpha\Gamma} \left(\frac{\partial R_{f_0}(f)}{\partial f_0} \frac{t_{\text{int}}}{N}\right)^2 \frac{Ndf}{\Delta f_{\text{win}}}\right)^{-1}. \quad (C7)$$

The integral runs over the frequency window. The approximation in the last step is valid when the frequency points are many ($N \gg 1$) and equally spaced.

Inserting Eqs. (C1) into (C7), the integral can be solved analytically, finally yielding

$$\delta f_0 = \sqrt{\mathbb{V}\left[\hat{f}_0\right]} = \frac{2\Gamma}{\epsilon\sqrt{R_o t_{\text{int}}}} \times \sqrt{\frac{\alpha}{\frac{\alpha^4 + \frac{8}{3} \times \alpha^3 - \alpha}{(1+\alpha^2)^3} + \arctan\alpha}}, \quad (C8)$$

where α is the relative window size. This expression is minimized for $\alpha \approx 1$. In that case, the square root evaluates to approximately unity as well. The ultimate sensitivity with least-squares fitting is thus

$$\eta_{\text{lstsq}}^{\text{opt}} = \delta f_0 \times \sqrt{t_{\text{int}}} \approx \frac{2\Gamma}{\epsilon\sqrt{R_0}}, \quad (C9)$$

similar to the optimum single-point sensitivity of amplitude detection, see Eq. (10) in the main text. Note that, in practice, this sensitivity is out of reach by a small factor. The reason is that resonance frequency is *not* the only quantity that must be estimated from the data. Robust estimation of also the contrast and the linewidth requires that the window is large enough to also capture the tails of the resonance ($\alpha \gtrsim 2$).

If the window is much larger than the linewidth ($\alpha \gg 1$, as required by wide-dynamic-range measurements), the square root in Eq. (C8) is approximately $\sqrt{2\alpha/\pi}$, meaning that the sensitivity is given by

$$\eta_{\text{lstsq}} \approx \frac{2\Gamma}{\epsilon\sqrt{R_0}} \times \sqrt{2\alpha/\pi}. \quad (C10)$$

This expression scales like $\sqrt{\alpha}$, which is intuitively plausible as only a fraction of the total integration time, of order t_{int}/α, is spent sampling the spectrum near the actual resonance line.

APPENDIX D: MAXIMUM RATE

We estimate an upper bound for the maximum tracking rate solely limited by the SNR. To get such a bound, we determine the integration t_{int} where the uncertainty in δf_0 [according to Eq. (A13)] becomes equal to the estimate δf_0^{rand} one would obtain if the phase were completely random over $[-\pi, \pi[$. Defining δf_0^{rand} by the square root of its variance,

$$\delta f_0^{\text{rand}} = \frac{\Delta f_{\text{win}}}{2\pi} \left[\frac{1}{2\pi}\int_{-\pi}^{\pi} d\phi \, \phi^2\right]^{1/2} = \frac{\Delta f_{\text{win}}}{\sqrt{3}}, \quad (D1)$$

setting $\delta f_0 = \delta f_0^{\text{rand}}$, and solving for t_{int}^{-1} we find that

$$t_{\text{int}}^{-1} = \frac{\epsilon^2 R_0 \pi^4}{6\alpha^2 \exp\left(\frac{2\pi}{\alpha}\right)}. \quad (D2)$$

Assuming numbers typical for our experiments ($\epsilon = 0.2$, $R_0 = 5 \times 10^5$ s^{-1}, $\Delta f_{\text{win}} = 30$ MHz, $\Gamma = 5$ MHz), we find that $t_{\text{int}}^{-1} = 4.4$ kHz.

On the other hand, the N-*V* center has a response time of approximately 1 μs [28]. For accurate sensing, the sweep period must be much larger than this, e.g., $t_{\text{int}} \gtrsim 100$ μs. This equally imposes a limit on the maximum sampling of the same order of magnitude.

APPENDIX E: DEMODULATION OF MAGNETIC FIELD GRADIENT

In the following we show how demodulating the luminescence signal at $f_{\text{TF}} \pm n f_{\text{mod}}$ gives access to the magnetic field gradient along the cantilever oscillation axis. In the presence of a magnetic gradient, the probe experiences an additional ac field, $B(t) = B_1 \cos(2\pi f_{\text{TF}} t)$, with $B_1 = x_0 \partial B / \partial x$, x_0 and f_{TF} being the cantilever oscillation amplitude and frequency, respectively, $\partial B / \partial x$ the field gradient along the oscillation axis, and B the vector component of the magnetic field along the N-*V* anisotropy axis.

In the absence of a magnetic field gradient, the luminescence signal is $R(t)$, as per Eq. (A2). With a nonzero field gradient, $R(t)$ incurs an additional phase modulation,

$$R'(t) = R\left(t + \frac{\Delta\phi}{2\pi f_{\text{mod}}} \cos(2\pi f_{\text{TF}} t)\right). \quad \text{(E1)}$$

Here the phase modulation depth is $\Delta\phi = \gamma_e B_1 / \Delta f_{\text{win}}$. In the limit of a small gradient ($\Delta\phi \ll 1$), we can expand Eq. (E1) to first order,

$$R'(t) \approx R(t) + \frac{dR(t)}{dt} \frac{\Delta\phi}{2\pi f_{\text{mod}}} \cos(2\pi f_{\text{TF}} t). \quad \text{(E2)}$$

The first term is simply the zero-gradient signal, from which we extract the static field as by demodulation at f_{mod}. The second term is an amplitude modulation of $dR(t)/dt$ at the frequency f_{TF}. We thus observe an up-converted version of $dR(t)/dt$ centered on f_{TF}.

Next, we express $R(t)$ as a Fourier series,

$$R(t) = \sum_{k=-\infty}^{\infty} a_k \exp(2\pi i k f_{\text{mod}} t), \quad \text{(E3)}$$

where $a_k \sim \exp(-\pi |k| / \alpha)$, see Eqs. (A4)–(A11). The time derivative is given by

$$\dot{R}(t) = 2\pi f_{\text{mod}} \sum_{k=-\infty}^{\infty} i k a_k \exp(2\pi i k f_{\text{mod}} t). \quad \text{(E4)}$$

We next rewrite the second term in Eq. (E2) as

$$\dot{R}(t) \frac{\Delta\phi}{2\pi f_{\text{mod}}} \cos(2\pi f_{\text{TF}} t) \quad \text{(E5)}$$

$$= \dot{R}(t) \frac{\Delta\phi}{2\pi f_{\text{mod}}} \text{Re}\left[\exp(2\pi i f_{\text{TF}} t)\right] \quad \text{(E6)}$$

$$= \frac{\Delta\phi}{2\pi f_{\text{mod}}} \times \text{Re}\left[\dot{R}(t) \exp(2\pi i f_{\text{TF}} t)\right] \quad \text{(E7)}$$

$$= \Delta\phi \times \text{Re}\left[\sum_{k=-\infty}^{\infty} i k a_k \exp\left(2\pi i (f_{\text{TF}} + k f_{\text{mod}})\right)\right]. \quad \text{(E8)}$$

Therefore, we expect spectral components at $f_{\text{TF}} + k f_{\text{mod}}$. Since a_k are known (by demodulation at $k f_{\text{mod}}$), measuring the amplitude of the $f_{\text{TF}} + k f_{\text{mod}}$ components will enable the inference of $\Delta\phi$, and thus, the gradient strength. Alternatively, the phase of the gradient signal itself also contains useful information about the static field, so the measurements of $k f_{\text{mod}}$ and $f_{\text{TF}} + k f_{\text{mod}}$ harmonics may be combined into a single estimate of both the field and the gradient.

[1] C. L. Degen, Scanning magnetic field microscope with a diamond single-spin sensor, Appl. Phys. Lett. **92**, 243111 (2008).

[2] G. Balasubramanian, I. Y. Chan, R. Kolesov, M. Al-Hmoud, J. Tisler, C. Shin, C. Kim, A. Wojcik, P. R. Hemmer, A. Krueger, T. Hanke, A. Leitenstorfer, R. Bratschitsch, F. Jelezko, and J. Wrachtrup, Nanoscale imaging magnetometry with diamond spins under ambient conditions, Nature **455**, 648 (2008).

[3] L. Rondin, J. P. Tetienne, P. Spinicelli, C. dal Savio, K. Karrai, G. Dantelle, A. Thiaville, S. Rohart, J. F. Roch, and V. Jacques, Nanoscale magnetic field mapping with a single spin scanning probe magnetometer, Appl. Phys. Lett. **100**, 153118 (2012).

[4] P. Maletinsky, S. Hong, M. S. Grinolds, B. Hausmann, M. D. Lukin, R. L. Walsworth, M. Loncar, and A. Yacoby, A robust scanning diamond sensor for nanoscale imaging with single nitrogen-vacancy centres, Nat. Nanotechnol. **7**, 320 (2012).

[5] L. Rondin, J. P. Tetienne, S. Rohart, A. Thiaville, T. Hingant, P. Spinicelli, J. F. Roch, and V. Jacques, Stray-field imaging of magnetic vortices with a single diamond spin, Nat. Commun. **4**, 2279 (2013).

[6] J. P. Tetienne, T. Hingant, J. Kim, L. H. Diez, J. P. Adam, K. Garcia, J. F. Roch, S. Rohart, A. Thiaville, D. Ravelosona, and V. Jacques, Nanoscale imaging and control of domain-wall hopping with a nitrogen-vacancy center microscope, Science **344**, 1366 (2014).

[7] J. P. Tetienne, T. Hingant, L. J. Martinez, S. Rohart, A. Thiaville, L. H. Diez, K. Garcia, J. P. Adam, J. V. Kim, J. F. Roch, I. M. Miron, G. Gaudin, L. Vila, B. Ocker, D. Ravelosona, and V. Jacques, The nature of domain walls

in ultrathin ferromagnets revealed by scanning nanomagnetometry, Nat. Commun. **6,** 6733 (2015).

[8] S. Vélez, J. Schaab, M. S. Wörnle, M. Müller, E. Gradauskaite, P. Welter, C. Gutgsell, C. Nistor, C. L. Degen, M. Trassin, M. Fiebig, and P. Gambardella, High-speed domain wall racetracks in a magnetic insulator, Nat. Commun. **10,** 4750 (2019).

[9] P. Appel, B. J. Shields, T. Kosub, N. Hedrich, R. Hubner, J. Fassbender, D. Makarov, and P. Maletinsky, Nanomagnetism of magnetoelectric granular thin-film antiferromagnets, Nano Lett. **19,** 1682 (2019).

[10] M. S. Wornle, P. Welter, Z. Kaspar, K. Olejnik, V. Novak, R. P. Campion, P. Wadley, T. Jungwirth, C. L. Degen, and P. Gambardella, Current-induced fragmentation of antiferromagnetic domains, (2019), ArXiv:1912.05287.

[11] M. S. Wornle, P. Welter, M. Giraldo, T. Lottermoser, M. Fiebig, P. Gambardella, and C. L. Degen, Coexistence of Bloch and Neél walls in a collinear antiferromagnet, Phys. Rev. B **103,** 094426 (2021).

[12] N. Hedrich, K. Wagner, O. V. Pylypovskyi, B. J. Shields, T. Kosub, D. D. Sheka, D. Makarov, and P. Maletinsky, Nanoscale mechanics of antiferromagnetic domain walls, Nat. Phys. **17,** 064007 (2021).

[13] A. Finco, A. Haykal, R. Tanos, F. Fabre, S. Chouaieb, W. Akhtar, I. Robert-Philip, W. Legrand, F. Ajejas, K. Bouzehouane, N. Reyren, T. Devolder, J. Adam, J. Kim, V. Cros, and V. Jacques, Imaging non-collinear antiferromagnetic textures via single spin relaxometry, Nat. Commun. **12,** 767 (2021).

[14] I. Gross, W. Akhtar, V. Garcia, L. J. Martinez, S. Chouaieb, K. Garcia, C. Carretero, B. Arthelemy, P. Appel, P. Maletinsky, J. V. Kim, J. Y. Chauleau, N. Jaouen, M. Viret, M. Bibes, S. Fusil, and V. Jacques, Real-space imaging of non-collinear antiferromagnetic order with a single-spin magnetometer, Nature **549,** 252 (2017).

[15] J. Chauleau, T. Chirac, S. Fusil, V. Garcia, W. Akhtar, J. Tranchida, P. Thibaudeau, I. Gross, C. Blouzon, A. Finco, M. Bibes, B. Dkhil, D. D. Khalyavin, P. Manuel, V. Jacques, N. Jaouen, and M. Viret, Electric and antiferromagnetic chiral textures at multiferroic domain walls, Nat. Mater. **19,** 386 (2020).

[16] L. Lorenzelli, Development of a scanning nitrogen-vacancy-center magnetometer for variable temperature experiments, PhD Thesis, ETH Zurich (2021), .

[17] Y. Dovzhenko, F. Casola, S. Schlotter, T. X. Zhou, F. Buttner, R. L. Walsworth, G. S. D. Beach, and A. Yacoby, Magnetostatic twists in room-temperature skyrmions explored by nitrogen-vacancy center spin texture reconstruction, Nat. Commun. **9,** 2712 (2018).

[18] I. Gross, W. Akhtar, A. Hrabec, J. Sampaio, L. J. Martinez, S. Chouaieb, B. J. Shields, P. Maletinsky, A. Thiaville, S. Rohart, and V. Jacques, Skyrmion morphology in ultrathin magnetic films, Phys. Rev. Mater. **2,** 024406 (2018).

[19] A. Jenkins, M. Pelliccione, G. Yu, X. Ma, X. Li, K. L. Wang, and A. C. B. Jayich, Single-spin sensing of domain-wall structure and dynamics in a thin-film skyrmion host, Phys. Rev. Mater. **3,** 083801 (2019).

[20] S. Velez, S. R. Gomez, J. Schaab, E. Gradauskaite, M. S. Wornle, P. Welter, B. J. Jacot, C. L. Degen, M. Trassin, M. Fiebig, and P. Gambardella, Current-driven dynamics and ratchet effect of skyrmion bubbles in a ferrimagnetic insulator, Nat. Nanotechnol. **17,** 834 (2022).

[21] L. Thiel, D. Rohner, M. Ganzhorn, P. Appel, E. Neu, B. Muller, R. Kleiner, D. Koelle, and P. Maletinsky, Quantitative nanoscale vortex imaging using a cryogenic quantum magnetometer, Nat. Nanotechnol. **11,** 677 (2016).

[22] M. Pelliccione, A. Jenkins, P. Ovartchaiyapong, C. Reetz, E. Emmanouilidou, N. Ni, and A. C. B. Jayich, Scanned probe imaging of nanoscale magnetism at cryogenic temperatures, Nat. Nanotechnol. **11,** 700 (2016).

[23] P. J. Scheidegger, S. Diesch, M. L. Palm, and C. L. Degen, Scanning nitrogen-vacancy magnetometry down to 350 mk, Appl. Phys. Lett. **120,** 224001 (2022).

[24] L. Thiel, Z. Wang, M. A. Tschudin, D. Rohner, I. Gutierrez-lezama, N. Ubrig, M. Gibertini, E. Giannini, A. F. Morpurgo, and P. Maletinsky, Probing magnetism in 2D materials at the nanoscale with single-spin microscopy, Science **364,** 973 (2019).

[25] Q. Sun, T. Song, E. Anderson, A. Brunner, J. Forster, T. Shalomayeva, T. Taniguchi, K. Watanabe, J. Grafe, R. Stohr, X. Xu, and J. Wrachtrup, Magnetic domains and domain wall pinning in atomically thin $CrBr_3$ revealed by nanoscale imaging, Nat. Commun. **12,** 1989 (2021).

[26] F. Fabre, A. Finco, A. Purbawati, A. Hadj-Azzem, N. Rougemaille, J. Coraux, I. Philip, and V. Jacques, Characterization of room-temperature in-plane magnetization in thin flakes of $CrTe_2$ with a single-spin magnetometer, Phys. Rev. Mater. **5,** 034008 (2021).

[27] R. Schirhagl, K. Chang, M. Loretz, and C. L. Degen, Nitrogen-vacancy centers in diamond: Nanoscale sensors for physics and biology, Annu. Rev. Phys. Chem. **65,** 83 (2014).

[28] R. S. Schoenfeld and W. Harneit, Real Time Magnetic Field Sensing and Imaging Using a Single Spin in Diamond, Phys. Rev. Lett. **106,** 030802 (2011).

[29] G. Kucsko, P. C. Maurer, N. Y. Yao, M. Kubo, H. J. Noh, P. K. Lo, H. Park, and M. D. Lukin, Nanometre-scale thermometry in a living cell, Nature **500,** 54 (2013).

[30] M. Parashar, A. Bathla, D. Shishir, A. Gokhale, S. Bandyopadhyay, and K. Saha, Sub-second temporal magnetic field microscopy using quantum defects in diamond, Sci. Rep. **12,** 8743 (2022).

[31] T. Haberle, D. Schmid-Lorch, K. Karrai, F. Reinhard, and J. Wrachtrup, High-Dynamic-Range Imaging of Nanoscale Magnetic Fields Using Optimal Control of a Single Qubit, Phys. Rev. Lett. **111,** 170801 (2013).

[32] C. J. Wang, R. Li, B. Ding, P. Wang, W. Wang, M. Wang, M. Guo, C. K. Duan, F. Shi, and J. Du, Single-spin scanning magnetic microscopy with radial basis function reconstruction algorithm, Appl. Phys. Lett. **116,** 184001 (2020).

[33] V. M. Acosta, E. Bauch, A. Jarmola, L. J. Zipp, M. P. Ledbetter, and D. Budker, Broadband magnetometry by infrared-absorption detection of nitrogen-vacancy ensembles in diamond, Appl. Phys. Lett. **97,** 174104 (2010).

[34] K. Arai, A. Kuwahata, D. Nishitani, I. Fujisaki, R. Matsuki, Y. Nishio, Z. Xin, X. Cao, Y. Hatano, S. Onoda, C. Shinei, M. Miyakawa, T. Taniguchi, M. Yamazaki, T. Teraji, T. Ohshima, M. Hatano, M. Sekino, and T. Iwasaki,

Millimetre-scale magnetocardiography of living rats with thoracotomy, Commun. Phys. **5**, 200 (2022).

[35] A. Gruber, A. Drabenstedt, C. Tietz, L. Fleury, J. Wrachtrup, and C. von Borczyskowski, Scanning confocal optical microscopy and magnetic resonance on single defect centers, Science **276**, 2012 (1997).

[36] V. Chechik, E. Carter, and D. Murphy, *Electron Paramagnetic Resonance, Oxford Chemistry Primers* (Oxford University Press, Oxford, 2016).

[37] F. Rice, A frequency-domain derivation of shot-noise, Am. J. Phys. **84**, 44 (2015).

[38] A. Dreau, M. Lesik, L. Rondin, P. Spinicelli, O. Arcizet, J. F. Roch, and V. Jacques, Avoiding power broadening in optically detected magnetic resonance of single NV defects for enhanced dc magnetic field sensitivity, Phys. Rev. B **84**, 195204 (2011).

[39] N. Moriya, *Primer to Kalman Filtering: A Physicist's Perspective, Engineering Tools, Techniques and Tables* (Nova Science Publishers, Hauppauge, New York, 2010).

[40] W. S. Huxter, M. L. Palm, M. L. Davis, P. Welter, C. H. Lambert, M. Trassin, and C. L. Degen, Scanning gradiometry with a single spin quantum magnetometer, Nat. Commun. **13**, 3761 (2022).

[41] F. P. Chmiel, N. W. Price, R. D. Johnson, A. D. Lamirand, J. Schad, G. V. der laan, D. T. Harris, J. Irwin, M. S. Rzchowski, C. Eom, and P. G. Radaelli, Observation of magnetic vortex pairs at room temperature in a planar α-Fe_2O_3/Co heterostructure, Nat. Mater. **17**, 581 (2018).